Check for updates

Intestinal explant barrier chip: long-term intestinal absorption screening in a novel microphysiological system using tissue explants†

Hossein Eslami Amirabadi, [iD] ‡[ab] Joanne M. Donkers, [iD] ‡[a] Esmée Wierenga,[a] Bastiaan Ingenhut,[c] Lisanne Pieters,[a] Lianne Stevens,[ad] Tim Donkers,[e] Joost Westerhout,[f] Rosalinde Masereeuw, [iD] [b] Ivana Bobeldijk-Pastorova,[a] Irene Nooijen[a] and Evita van de Steeg*[a]

The majority of intestinal *in vitro* screening models use cell lines that do not reflect the complexity of the human intestinal tract and hence often fail to accurately predict intestinal drug absorption. Tissue explants have intact intestinal architecture and cell type diversity, but show short viability in static conditions. Here, we present a medium throughput microphysiological system, Intestinal Explant Barrier Chip (IEBC), that creates a dynamic microfluidic microenvironment and prolongs tissue viability. Using a snap fit mechanism, we successfully incorporated human and porcine colon tissue explants and studied tissue functionality, integrity and viability for 24 hours. With a proper distinction of transcellular over paracellular transport (ratio >2), tissue functionality was good at early and late timepoints. Low leakage of FITC–dextran and preserved intracellular lactate dehydrogenase levels indicate maintained tissue integrity and viability, respectively. From a selection of low to high permeability drugs, 6 out of 7 properly ranked according to their fraction absorbed. In conclusion, the IEBC is a novel screening platform benefitting from the complexity of tissue explants and the flow in microfluidic chips.

Introduction

In drug development, oral bioavailability and intestinal drug metabolism are poorly predicted in the preclinical phase, as the majority of conventional intestinal screening models do not reflect the complex physiology of the human intestinal tract.[1–3] The lack of accurate preclinical drug screening models prevents the majority of drug candidates from reaching clinical approval and brings high costs for the pharmaceutical industry to deliver novel therapeutics to the market. Likewise, the nutrition industry, which increasingly tests (mixtures of) food ingredients *in vitro*, is still looking for models that better represent the intestinal architecture and its microenvironment.

Currently, a diverse range of *in vitro* and *in vivo* models are used to study intestinal barrier function and drug absorption.[4–6] While *in vivo* models represent the intestinal architecture and microenvironment more accurately, they coincide with serious shortcomings such as interspecies differences, low throughput, high costs and ethical issues.[7] *In vitro* cell-based assays are therefore often used as a higher throughput and cheaper alternative.[1] A conventional approach in intestinal absorption studies is to grow immortalized cell lines, such as Caco-2 and HT-29, on a porous membrane between two compartments, *e.g.* Transwell inserts.[8,9] Although well established, these models are limited in mimicking absorption in the gastrointestinal tract with their 2D structure and monocellular phenotype.[10,11] In addition, they lack the dynamic microenvironment of the intestine, *e.g.* fluid shear stress, and require long differentiation times.[12] Recent advances in biofabrication and organoid technologies have led to more physiological 3D intestinal barrier models with multiple cell types.[13,14] Innovations in microfluidic technology has added dynamic microenvironments and automatic delivery of nutrients, drugs and even microbiome to so called intestine on a chip

a Department of Metabolic Health Research, The Netherlands Organization for Applied Scientific Research (TNO), Zeist, The Netherlands.
E-mail: evita.vandesteeg@tno.nl
b Division of Pharmacology, Utrecht Institute for Pharmaceutical Sciences, Utrecht University, Utrecht, The Netherlands
c Materials solution department, TNO, and Brightlands Materials Centre, Geleen, The Netherlands
d Department of Surgery, Division of Transplantation, Leiden University Medical Centre, Leiden, The Netherlands
e Division of Space systems engineering, TNO, Delft, the Netherlands
f RAPID, TNO, Utrecht, the Netherlands

† Electronic supplementary information (ESI) available. See DOI: 10.1039/d1lc00669j
‡ These authors contributed equally: Hossein Eslami Amirabadi and Joanne M. Donkers.

devices.[15,16] Many of these microphysiological systems are able to replicate different aspects of the intestinal physiology in health and disease using human stem cell derived organoids.[17,18] Other systems use co-cultures of different intestinal epithelial cell lines to better resemble normal gut physiology,[19–21] or even add a digestion compartment to mimic the process before intestinal absorption and thereby improve the prediction of drug oral bioavailability.[20,22] While highly appealing, these cultures are still not very relevant in intestinal drug absorption screening, as they still lack the complex and mature intestinal tissue architecture. Furthermore, the used microfluidic platforms show a low throughput and high complexity, and often use silicone-based materials that show variable adsorption of pharmaceutical compounds.[23,24]

Ex vivo models, such as the Ussing chamber, use human tissue explants and offer more complexity in the tissue architecture.[25] These models can reveal regional and interspecies differences of intestinal absorption and, unlike cell-based *in vitro* models, show promising results for moderately and poorly absorbed drugs.[26] Our InTESTine™ system takes this one step further and allows *ex vivo* absorption assays in a higher throughput wells plate format.[27–29] However, the human tissue explants in these platforms have a relatively short viability (max. 6 h) and are, therefore, not applicable to study tissue functionality and absorption for longer term. Processing the tissue explants into organotypic slices has demonstrated that tissue viability could be maintained longer[30,31] but this technique has so far not been used as a barrier model to study intestinal absorption. Sustained viability (≥ 24 h) of unsliced tissue explants was shown upon exposure to microfluidic flow.[32–35] However, only the systems of Dawson *et al.*,[35] and Richardson *et al.*,[34] had a design with two-sided and separated flow to the apical and basolateral side of the tissue explant, a requirement for drug permeability studies. Here, we present our novel microfluidic chip the Intestinal Explant Barrier Chip (IEBC), which incorporates intestinal tissue explants in a two microchannel setup without cross contamination between the microchannels, thereby simulating a dynamic *in vivo* like microenvironment. Using high resolution stereolithography 3D printing, we were able to create complex mechanical mechanisms in the chip. We successfully mounted human and porcine colon tissue explants in the IEBC, applied fluid flow on both sides of the tissue for 24 hours and characterized the effect of different flow rates on the functionality, barrier integrity and viability of the tissue segments. The apparent permeability (P_{app}) rates of the intestinal tissue remained stable during the 24 hours and properly ranked high to low permeability drugs. The microfluidic system, including the chip, showed very low non-specific binding of drugs. Our system offers a medium throughput method to study intestinal absorption of drugs *ex vivo* and provides an unprecedented opportunity to perform more complex experiments with tissue explants.

Results

Design and characterization of the Intestinal Explant Barrier Chip

To fix tissue explants between two microchannels, we designed a snap fit mechanism in the IEBC (Fig. 1a–c), consisting of eight flexible cantilevers, a rubber sealing ring and a fixing insert. First, we placed the tissue on a support mesh and placed them in the chip. The larger end of a 1 ml pipette tip can then be used to push down the fixing insert on the tissue and the rubber with around 24 N (2.4 kg) force until the hook on the insert clicks below the hook of the cantilever (Fig. 1b and c). While fixed, this mechanism applies force on the rubber ring to prevent leakage through the sides of the tissue. The tissue explant is inserted through an opening on top of the chip, separated from the inlets and outlets, to avoid trapping bubbles. Afterwards, we carefully closed the chip with a 3D printed removable cap.

We optimized the dimensions and the number of the cantilevers, so they are flexible enough to deflect and at the same time sufficiently strong to hold the assembly in place. Fig. 1d shows the solid stress levels on a single cantilever when the tissue explant is fixed. The elastic modulus and the maximum strength were found with a tensile test (ESI† Table S1). For different thicknesses of the tissue, different insert sizes can be used to maintain the stress levels on the cantilever well below its maximum strength while keeping enough force on the rubber to prevent any leakage from the side of the explant. Fig. S1† demonstrates that the maximum stress occurs on the corners of the inner surface of the cantilever, which is shown as a function of the tissue thickness. Because micro-cracks could potentially appear in the cantilevers after fixing and removing tissue explants, we did not reuse the chips.

We used a stereolithography (SLA) 3D printer to fabricate the mechanisms in the chip. The higher resolution of the SLA printing than conventional 3D printing techniques also allowed us to print standard fluidic ports on the chip, such as barbed connectors or threaded holes for finger tight connectors (ESI† Fig. S2a†). The ports connected the chip to a microfluidic recirculation system where a peristaltic pump recirculated media on both sides of the tissue explant (Fig. 1e and ESI† Fig. S2b). Each system consisted of 4 chips and each chip had two channels connected to the pump (one apical and one basolateral). Multiple systems, with 4 chips each, can run in parallel with a maximum throughput of 28 chips in one experiment. Furthermore, 3D printed microfluidic reservoirs provided an injection and sampling point within the microfluidic recirculation system. The distance between the reservoirs was similar to the wells in a 96-well plate that enabled us to use multichannel pipettes to sample from and inject to the reservoirs (ESI† Fig. S2c). A short set of tubings connected the reservoirs to the chip which minimized the chance of trapping bubbles in this sensitive region of the microfluidic system. The largest flow rate tested in the system was 50 mL h^{-1} above which would
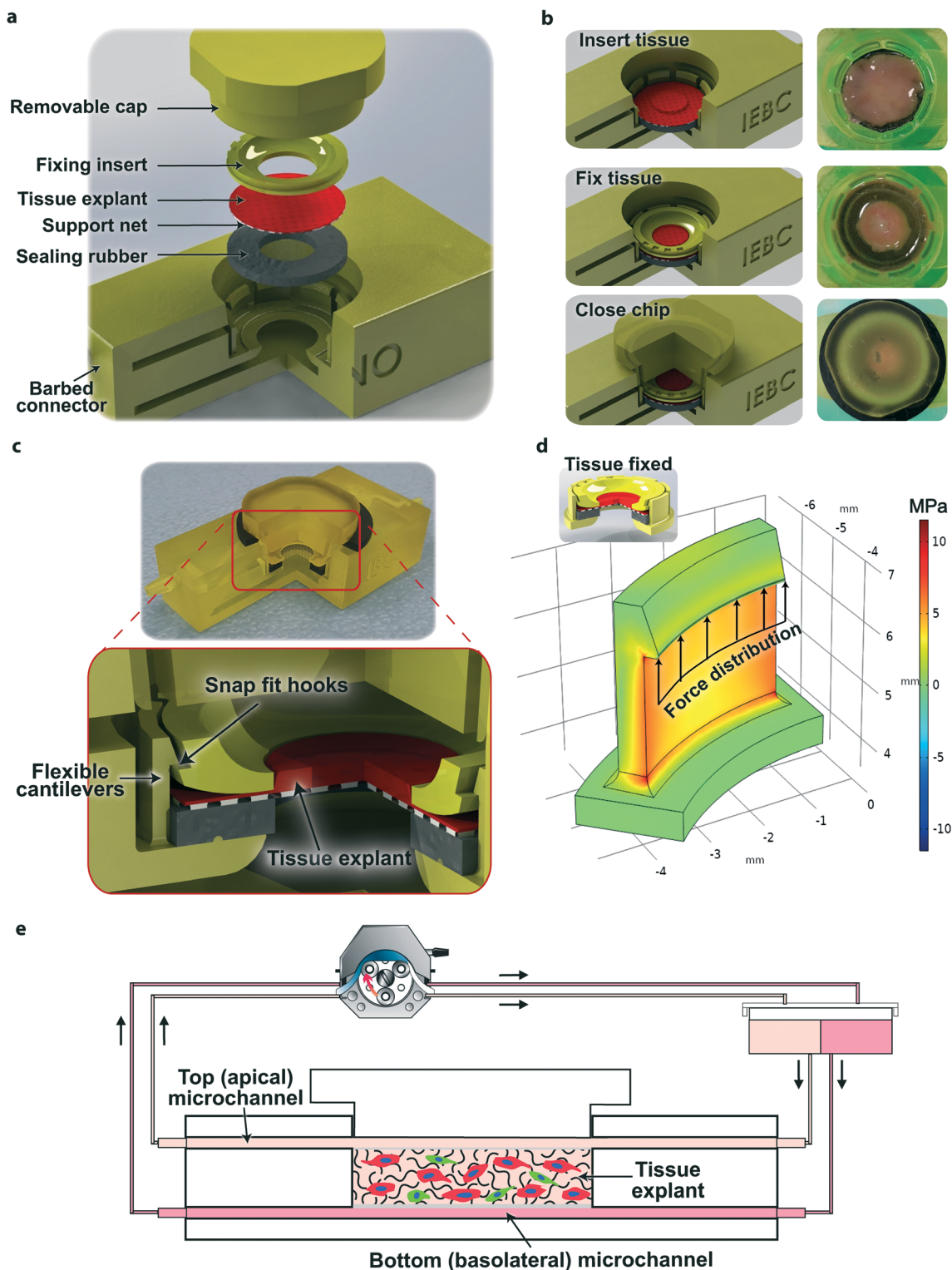
Fig. 1 A schematic overview of the Intestine Explant Barrier Chip (IEBC). **a**, An exploded view of the IEBC cross section with different parts to insert the tissue and close the chip. **b**, Steps to fix the tissue in the IEBC and close the chip. When placing a tissue explant in the IEBC, first a rubber ring is placed in the central well of the chip, followed by the tissue on a supporting mesh and a fixing insert, and finally the chip is closed with a cap. **c**, 3D printed IEBC (cross section) demonstrating the assembled tissue explant inside the chip. The lower image demonstrates how the snap fit mechanism works. **d**, Mechanical analysis of a single flexible cantilever, using COMSOL Multiphysics, while the tissue explant is fixed in the snap fit mechanism (right). Color contour plots show the distribution of Von Mises stresses on the outer surface of the cantilever when the rubber is deformed 100 μm. **e**, Schematic overview of the IEBC microfluidic recirculation system. All media are added to the reservoirs. The peristaltic pump withdraws the media from the reservoirs through the chip and recirculates them back to the reservoirs. In the IEBC, the tissue explant is placed between two microchannels that represent the apical and basolateral sides in the intestine.

create non-physiological shear stress on the intestinal explant. The largest pressure difference with this flow rate between inside and outside the chip was low (approximately 0.4 mbar). We used a support mesh with openings of 250 μm and porosity of 50% for the explants.

To ensure biocompatibility, the chip was printed from a resin used in dental applications.[36] To verify the suitability of the material of our chip for these studies, we measured the recovery of seven marketed and FDA approved drugs. After 20 hours recirculation through the IEBC with porcine colon explants, the average recovery of the drugs from the system was more than 90% for acyclovir, metformin, atenolol, mannitol, and more than 86% for warfarin, caffeine and antipyrine (Table 1). The residual amount of drugs in the tissue was less than 1% (Table S2†). These results support the applicability of the IEBC for intestinal transport studies of small molecules without losing a large fraction of the test drugs due to non-specific binding (adsorption) or uptake (absorption) by the materials used in the microfluidic system.

Higher flow rate increases oxygen supply without affecting tissue viability

To assess the effect of fluid flow on colon explants and their liquid environment, we ran experiments at two different flow rates: 2 and 20 mL h^{-1}. Fluid flow simulations in the apical microchannel showed that the shear stress on the tissue explant was $3.5 \pm 0.5 \times 10^{-4}$ and $3.5 \pm 0.5 \times 10^{-3}$ dyne per cm^2 for 2 and 20 mL h^{-1}, respectively (Fig. 2a and S3†). These values were similar to the theoretical shear stress of laminar flow with a parabolic velocity profile on the bottom of a rectangular microchannel, with the same height as the apical microchannel (dashed lines in the graph in Fig. 2a). To assess the effect of flow rate on tissue viability, lactate dehydrogenase (LDH) secretion into the apical and basolateral compartments was measured over time and intracellular LDH levels were determined after 24 hours of incubation. Previously, an LDH release of <4% h^{-1} was reported for human intestinal tissue explants mounted in the static InTESTine™ model.[27] In the IEBC, cumulative LDH release from human colon explants was only $15.8 \pm 3.8\%$ over 24 hours (0.66% h^{-1}) in the low flow rate incubation (Fig. 2b). The higher flow rate of 20 mL h^{-1} almost doubled the amount of released LDH ($27.0 \pm 3.0\%$, 1.12% h^{-1}). Nevertheless, endpoint intracellular LDH levels were comparable to the intracellular LDH levels at the start of the incubation for both flow rates (Fig. 2c), showing that the tissue remained viable, metabolically active and maintained its intracellular LDH levels under flow in the IEBC. Histological staining of porcine colon tissue explants before and 24 hours after incubation in the IEBC confirmed that the tissue remained intact for both flow rates, showing a clear mucosal layer, including an epithelial layer with gland invaginations, muscularis mucosa and submucosa (Fig. 2d).

Experiments in the static Ussing chamber have shown that the oxygen concentration in the medium decreases over time due to the consumption of oxygen by the tissue.[37,38] However, a microfluidic setup continuously refreshes medium, and thus oxygen supply, around the tissue. For example, at a flow rate of 2 mL h^{-1} the medium can pass the tissue up to 14 times in an IEBC experiment. We evaluated how flow rate and sampling affected the oxygen concentration in the apical medium in contact with intestinal tissue explants in the IEBC. To do so, we modified the cap of the chip to use a non-invasive oxygen sensor plug (a plug and play mini-luer, Fig. 3a and S4a†). An optical fiber connected the sensor plug to an oxygen meter outside the incubator (oxygen level in the incubator was similar to atmospheric air). Experiments applying high flow rate (20 mL h^{-1}) in the IEBC showed an average oxygen level of 19.5–20.0% in the apical compartment (both with and without tissue), whereas the average oxygen concentration in the apical medium on top of porcine colon intestinal tissue segments was 3–5% lower for the low flow rate (2 mL h^{-1}; Fig. 3b, individual data in Fig. S4b†). This difference can be explained by oxygen consumption by the tissue and incomplete refreshment of the medium under low flow rate condition, as the oxygen concentration was similar between both flow rates without tissue. The oxygen concentrations in the apical compartment under low flow rate condition, however, appeared sufficient to maintain tissue viability (Fig. 2b–d). During sampling and redosing, slight drops in the measured oxygen concentration were seen, both with and without tissue present, likely caused by a temperature drop in the incubator (through opening of the door).[39] A more substantial decrease in the oxygen concentration at these timepoints was observed for incubations with tissue resulting from oxygen consumption.

Table 1 Recovery of test drugs in the IEBC with porcine tissue

Test compound	t = 20 hours (%)
Acyclovir	92.4 ± 0.9
Metformin	92.2 ± 0.5
Atenolol	91.5 ± 0.9
Mannitol	91.2 ± 2.0
Warfarin	88.2 ± 2.0
Caffeine	87.6 ± 2.0
Antipyrine	86.0 ± 0.9

Compounds were ranked based on their recovery. Radiolabeled test compounds (^{14}C for warfarin, metformin, acyclovir, antipyrine, caffeine or ^{3}H for atenolol, mannitol) were administered apically and radioactivity in the apical and basolateral compartments was measured after 20 h. Medium was refreshed at 20 h. To calculate the drug recovery, total radioactivity at t = 20 h was compared to the starting dose at t = 0. Data are represented as mean ± SEM (warfarin, metformin and acyclovir: n = 4–7 from 2 independent experiments; antipyrine, atenolol, caffeine and mannitol: n = 8–10 from 3 independent experiments). n.d. = not determined.
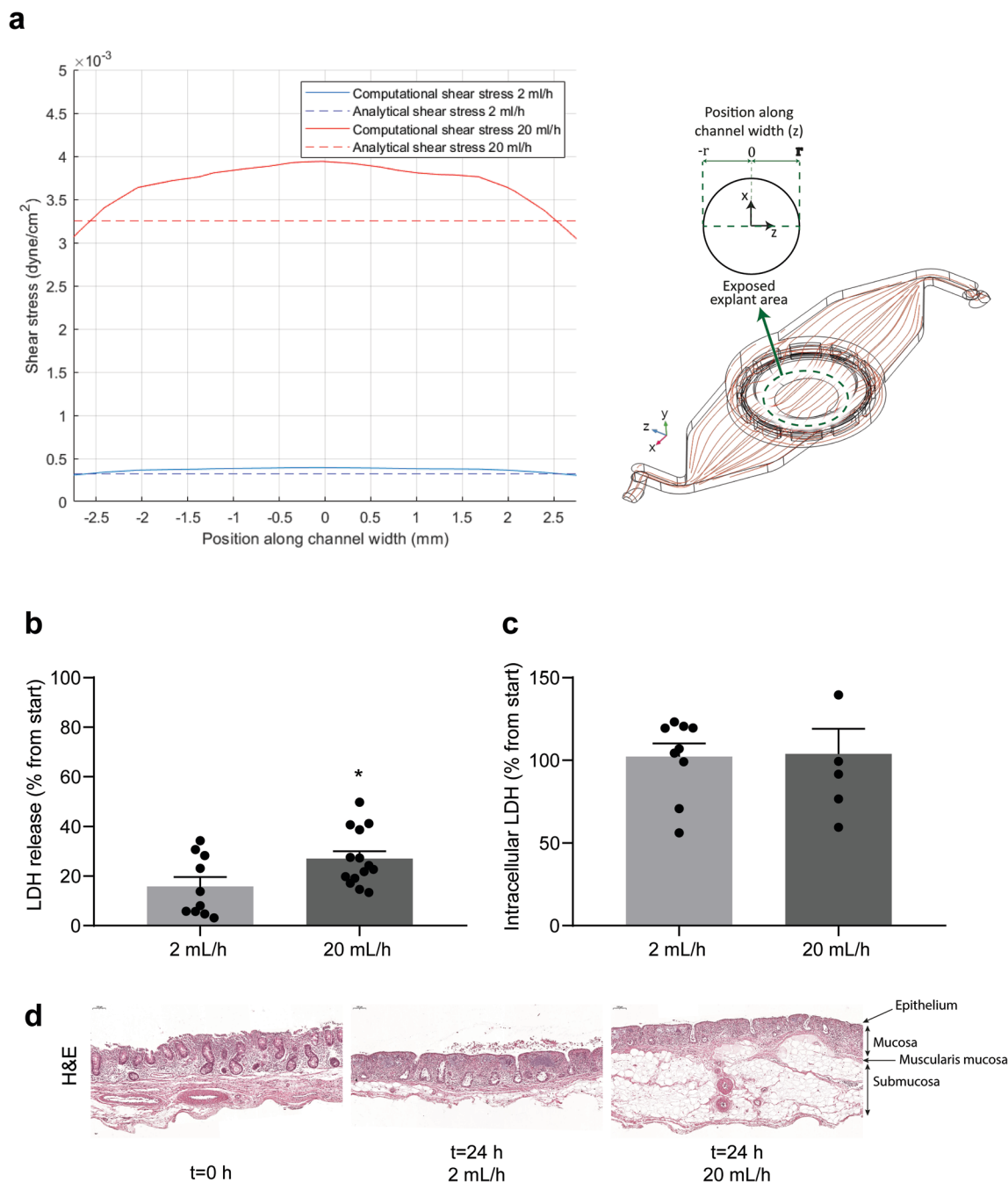
Human colon tissue explants show sustained integrity and functionality

Upon intact barrier integrity, intestinal tissue explants show low apical to basolateral leakage of a large, inert molecule,

Fig. 2 Shear stress and viability of the tissue explant in the IEBC at different flow rates. **a**, Simulated shear stress on the tissue explant in the apical (top) channel for flow rates of 2 mL h^{-1} and 20 mL h^{-1}. Computational values for the shear stress and the streamlines were derived from COMSOL flow simulations. For the analytical values, shear stress was derived from the parabolic velocity profile of a laminar flow on the bottom of a rectangular channel with the same height and width of the apical channel at the site of the tissue explant. **b** and **c**, human colon tissue explants were mounted in the IEBC and exposed to a flow rate of 2 or 20 mL h^{-1} for 24 hours. Cumulative LDH release into the apical and basolateral compartments ($n = 10$–14) (b) and intracellular LDH levels ($n = 5$–9) (c) in human colon tissue explants were determined after 24 hours and compared to the original level of intracellular LDH at $t = 0$. Data are presented as mean + SEM. **d**, Tissue morphology (H&E staining) of porcine colon tissue explants at $t = 0$ or after 24 hours exposure to a flow rate of 2 or 20 mL h^{-1} (representative images of $n = 4$). Arrows indicate the intestinal layers. * $p < 0.05$, calculated by Students t-test.

such as fluorescent dextran 4 kDa (FD4). In the IEBC, FD4 P_{app} was the same ($\approx 1 \times 10^{-6}$ cm s^{-1}) for human colon tissue exposed to low (2 mL h^{-1}) and high (20 mL h^{-1}) flow rates and remained stable over time (Fig. 4a). Expressed as % h^{-1}

(Fig. S5a†), FD4 permeability remained below the cut-off value of <1% h^{-1}, corresponding to a P_{app} value of $\approx 52.5 \times 10^{-6}$ cm s^{-1}, as was set for the static InTESTine™ model by Stevens *et al.*[27] A 10–15 fold higher P_{app} for FD4 in the IEBC
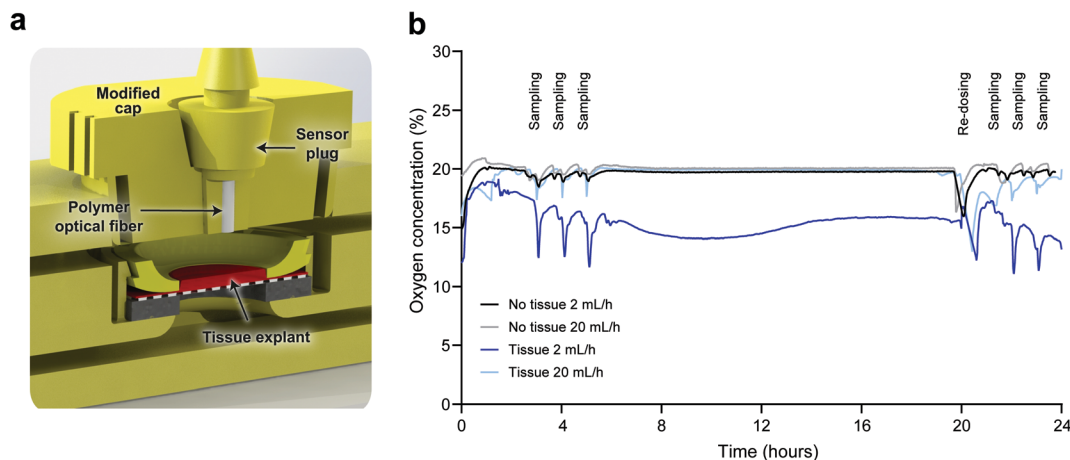
Fig. 3 Oxygen concentration in the IEBC. **a**, The cap of the microfluidic chip was modified to fit a sensor plug, connected to an optical fiber. The connection between the sensor plug and the modified cap was tight enough to prevent any leakage during the experiment. **b**, Oxygen concentration in the apical medium on top of porcine colon tissue explants in the IEBC or empty chips (without tissue) exposed to a flow rate of 2 or 20 mL h^{-1} for 24 hours. Oxygen concentrations were measured with one minute intervals, data represents the average (n = 5 for IEBC with tissue, n = 2–3 for IEBC without tissue). Results for the individual IEBCs are presented in ESI† Fig. S4b.
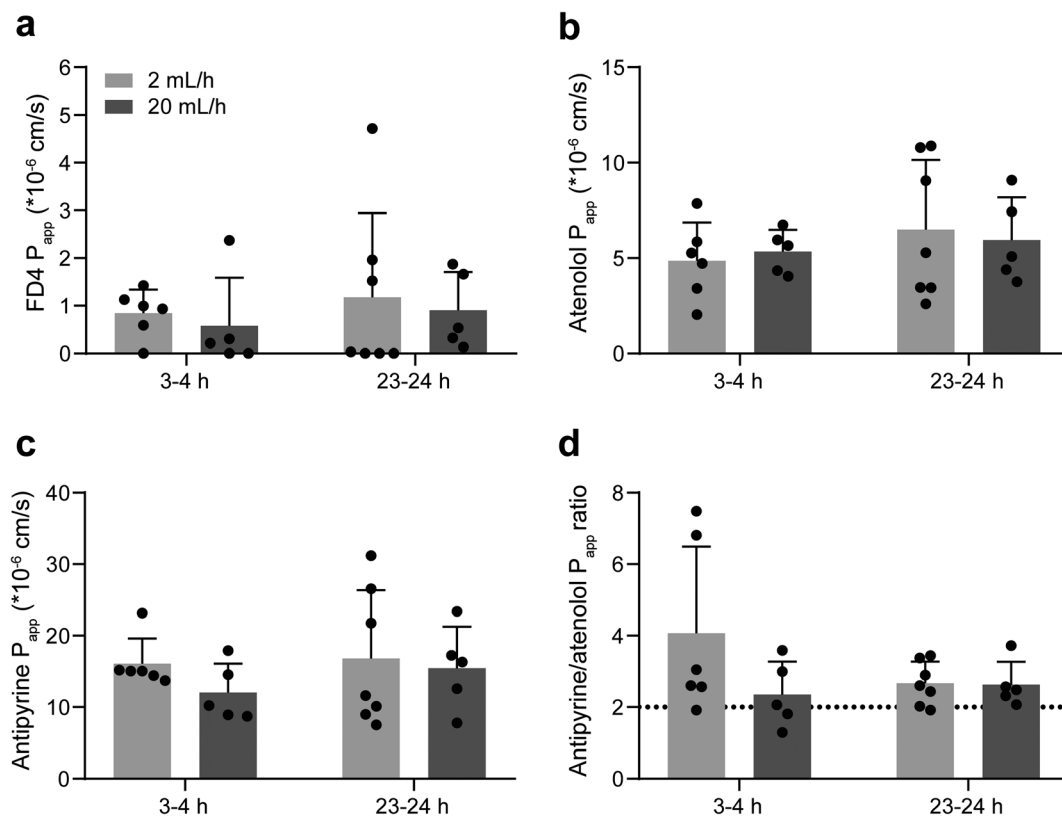

Fig. 4 Integrity and functionality of the tissue explant in the IEBC. Human colon tissue explants were mounted in the IEBC and exposed to a flow rate of 2 or 20 mL h^{-1} for 24 hours (n = 5–7/group, data collected from 4 independent experiments). a–c, Apparent permeability (P_{app}) of FITC-dextran-4000 (FD4, 50 μM) (a), atenolol (10 μM) (b), and antipyrine (10 μM) (c) were determined between 3–4 hours and 23–24 hours. **d**, Ratio of transcellular transport (P_{app} antipyrine) to paracellular transport (P_{app} atenolol). Dotted line indicates a P_{app} ratio of 2 which is set as a cut-off value in the static InTESTine™ model by Stevens *et al.*[27] Data are presented as mean + SEM.

without tissue (Fig. S5b and c†) further confirmed intact barrier function of the intestinal tissue explants. In the same explants, we analyzed the transport of two small molecule model drugs to study intestinal permeability: atenolol and antipyrine.[40] Atenolol is a moderately permeable drug (≈50% fraction absorbed (Fa)) and translocates *via* the paracellular
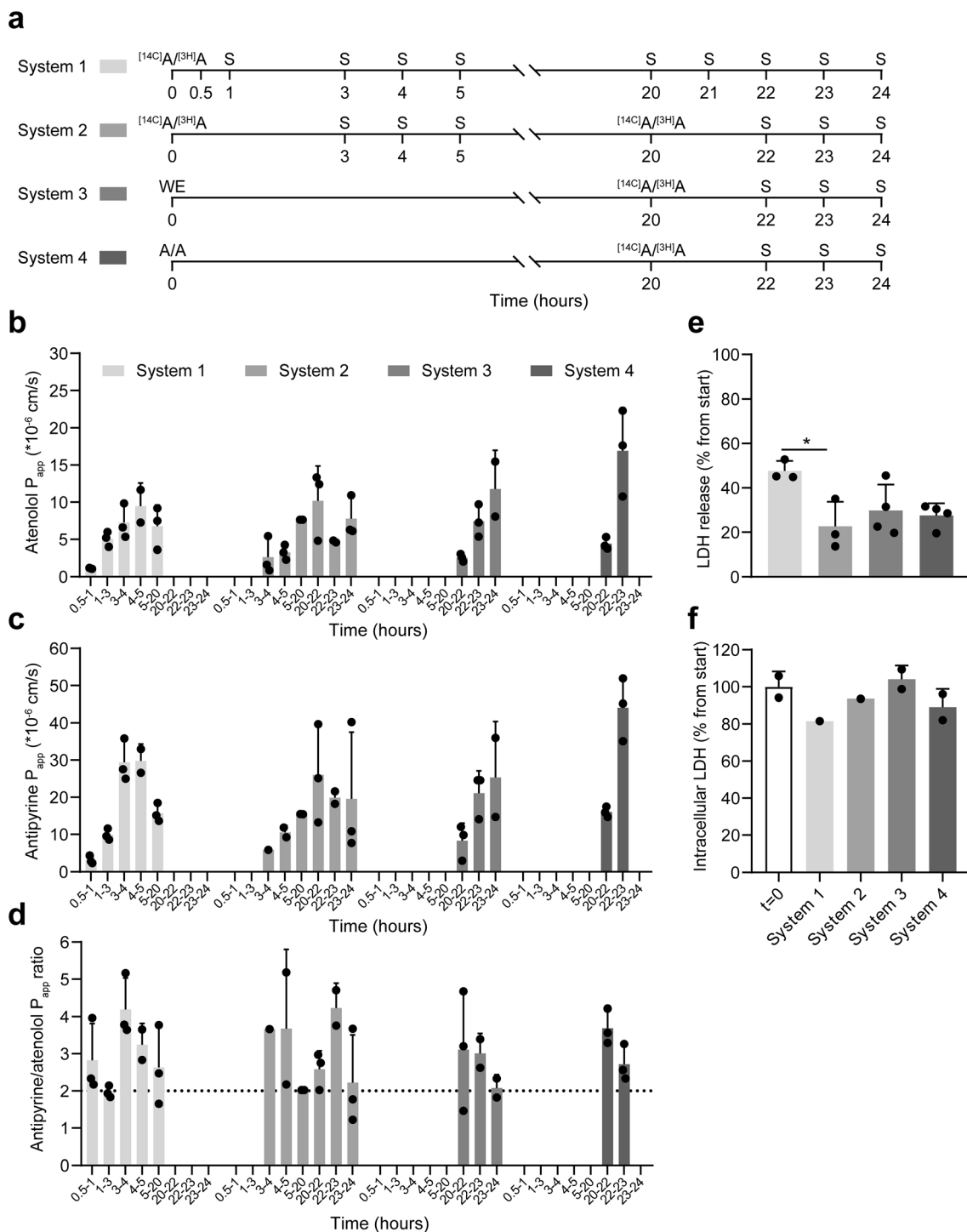
Fig. 5 Impact of timing of compound administration on tissue performance in the IEBC. a, Schematic overview of the 4 different experimental setups. In each system, 4 IEBC chips were mounted with porcine colon tissue explants and exposed to a flow rate of 2 mL h^{-1} for 24 hours. Apical dose solution contained radiolabeled antipyrine ($^{[14C]}$A) and atenolol ($^{[3H]}$A), unlabeled antipyrine and atenolol (A/A) or no compounds (WE) at the start of the experiment. Sampling (S) was performed at indicated timepoints. Replacement of the dose solution with medium containing $^{[14C]}$A and $^{[3H]}$A occurred after 20 hours in systems 2–4. b and c, P_{app} of atenolol (10 μM) (b) and antipyrine (10 μM) (c) were determined between multiple time points. d, Ratio of transcellular transport (P_{app} antipyrine) over paracellular transport (P_{app} atenolol). Dotted line indicates a P_{app} ratio of 2. e, Cumulative LDH release into the apical and basolateral compartments was determined after 24 hours and compared to the level of intracellular LDH at $t = 0$. f, Intracellular LDH levels ($n = 1$–2/system) were determined after 24 hours and compared to the level of intracellular LDH at $t=0$. Data are presented as mean + SD.

route, while antipyrine is a highly permeable drug (100% Fa) that translocates *via* the transcellular route. P_{app} values of antipyrine are consequently expected to be about 2-fold higher than the P_{app} values of atenolol.[27] With P_{app} values between 4.8–6.5 × 10^{-6} cm s^{-1} for atenolol and 12.0–16.8 × 10^{-6} cm s^{-1} for antipyrine (Fig. 4b and c), transport of both compounds was comparable between the two flow rates and different timepoints. With a mean antipyrine/atenolol P_{app} ratio above 2 for all conditions and timepoints (Fig. 4d), the functionality of human colon tissue explants in the IEBC was good and stable during the 24 hours experiment. In a separate study, we used two other model drugs, mannitol (<50% Fa, moderate permeability) and caffeine (100% Fa, high permeability), to further assess the functionality of human colon tissue in the IEBC using the two flow rates. FD4 leakage was low and remained below the maximum permeability threshold of 1% h^{-1}, with P_{app} values below 2 × 10^{-6} cm s^{-1} for both flow rates between 3–4 hours and slightly higher P_{app} values of 2.6 × 10^{-6} cm s^{-1} or 5.9 × 10^{-6} cm s^{-1} between 23–24 hours for the low and high flow rates, respectively (Fig. S5d–f†). The mean caffeine/mannitol P_{app} ratio was above 2 for both flow rates between 3–4 hours and for the low flow rate between 23–24 hours, showing good and endured tissue functionality in these conditions (Fig. S5g†). With 1.63 ± 0.38, the caffeine/mannitol P_{app} ratio did not meet the criterion of 2 for the high flow rate of 20 mL h^{-1} between 23–24 hours.

Dose timing affects transport rates but not the antipyrine/atenolol transport ratio

To assess the stability of small molecule transport rates further and to investigate if the timing of (radiolabeled) compound administration affected these rates, we compared four different experimental setups using porcine colon tissue in the IEBC (Fig. 5a). Radiolabeled antipyrine ([14C]A) and atenolol ([3H]A) were applied as model compounds. Early transport effects were assessed in system 1, as well as the difference with redosing after 20 hours as applied in systems 2–4. System 2 supplied [14C]A and [3H]A from the start of the experiment, while systems 3 and 4 started with medium without the drugs or medium with non-radiolabeled antipyrine and atenolol, respectively, to evaluate the effect of the starting medium on the results obtained between 20–24 hours. Of note, the setup of the human colon tissue experiments in the previous section was most similar to the setup of system 2, except for less sampling timepoints and these experiments were not exposed to radiolabeled compounds between 4–20 hours. No data was obtained for the last 3 timeframes of system 1 and the last hour of system 4. FD4 leakage was low and comparable between all systems, with system 2 showing the lowest FD4 permeability and the least variability between the replicates (Fig. S6a and b†). In the first system, transport of both compounds was very low between 30–60 minutes (P_{app} atenolol 1.1 × 10^{-6} cm s^{-1}; P_{app} antipyrine 3.1 × 10^{-6} cm s^{-1}), which increased between 60–

180 minutes (P_{app} atenolol 5.1 × 10^{-6} cm s^{-1}; P_{app} antipyrine 9.9 × 10^{-6} cm s^{-1}) and subsequently stabilized to a P_{app} of 6.8–9.5 × 10^{-6} cm s^{-1} for atenolol and 15.7–29.7 × 10^{-6} cm s^{-1} for antipyrine (Fig. 5b and c). Despite the lower transport at the early timepoints, antipyrine/atenolol P_{app} ratio was >2 at all timepoints (Fig. 5d), indicating good tissue functionality from the start of the experiment onwards. We observed a similar phenomenon in systems 3 and 4 early after the radiolabeled compound administration (20–22 hours). Thereafter, atenolol and antipyrine transport stabilized to a P_{app} of ≈10 × 10^{-6} cm s^{-1} for atenolol and ≈30 × 10^{-6} cm s^{-1} for antipyrine 3 hours after radiolabeled compound administration. This stabilization did not depend on the presence of radiolabeled compounds (system 2), non-radiolabeled compounds (systems 4) or no compounds (systems 3) at t = 0 h. Again, similar to system 1, regardless of low transport at early timepoints after dosing or more stabilized transport at later timepoints, systems 2–4 had antipyrine/atenolol P_{app} ratios >2 during the whole experiment. In contrast to system 1, redosing after 20 hours in systems 2–4 gave us the advantage to correct for technical irregularities that occurred overnight which improved data collection afterwards. By measuring the total LDH secretion into the apical and basolateral compartments, we assessed the effect of the different experimental setups on tissue viability. Total LDH secretion was highest in system 1 (47.6%, Fig. 5e) while system 2 showed the lowest level of LDH secretion (22.6%), suggesting that the tissue viability was the least affected in the latter setup. The LDH secretion in systems 3 and 4 was more comparable to system 2 than to system 1 but showed no significant differences with the latter. Lower levels of intracellular LDH in system 1 (81.6%, Fig. 5f), compared to the well-preserved intracellular LDH levels for system 2–4 (≈90–100%) also suggest that tissue viability was sustained better in the latter 3 systems.

IEBC P_{app} follows drug ranking based on their permeability

So far, the IEBC confirmed high or low permeability of antipyrine and caffeine or atenolol and mannitol, respectively. By acquiring warfarin, metformin and acyclovir transport data in porcine colon tissue, using the experimental setup of system 2 (Fig. 5a), we expanded this first dataset of high to low permeability drugs in the IEBC. As for atenolol and antipyrine, warfarin, metformin and acyclovir P_{app} were rather stable during the experiment (Fig. 6a). The highest variability was seen for warfarin, which was reduced when using a higher flow rate (Fig. S7a†). Low FD4 permeability confirmed intact tissue barrier integrity (Fig. 6b and c and S7b and c†) and comparable levels of secreted LDH to previous experiments affirmed that none of the 3 drugs showed adverse effects on the tissue (Fig. 6d and S7d†). Interestingly, the total LDH secretion was higher in one of the two experiments (open *vs.* closed dots), but this was not reflected by differences in intracellular LDH levels after 24 hours (Fig. S7e†), suggesting interindividual/inter-
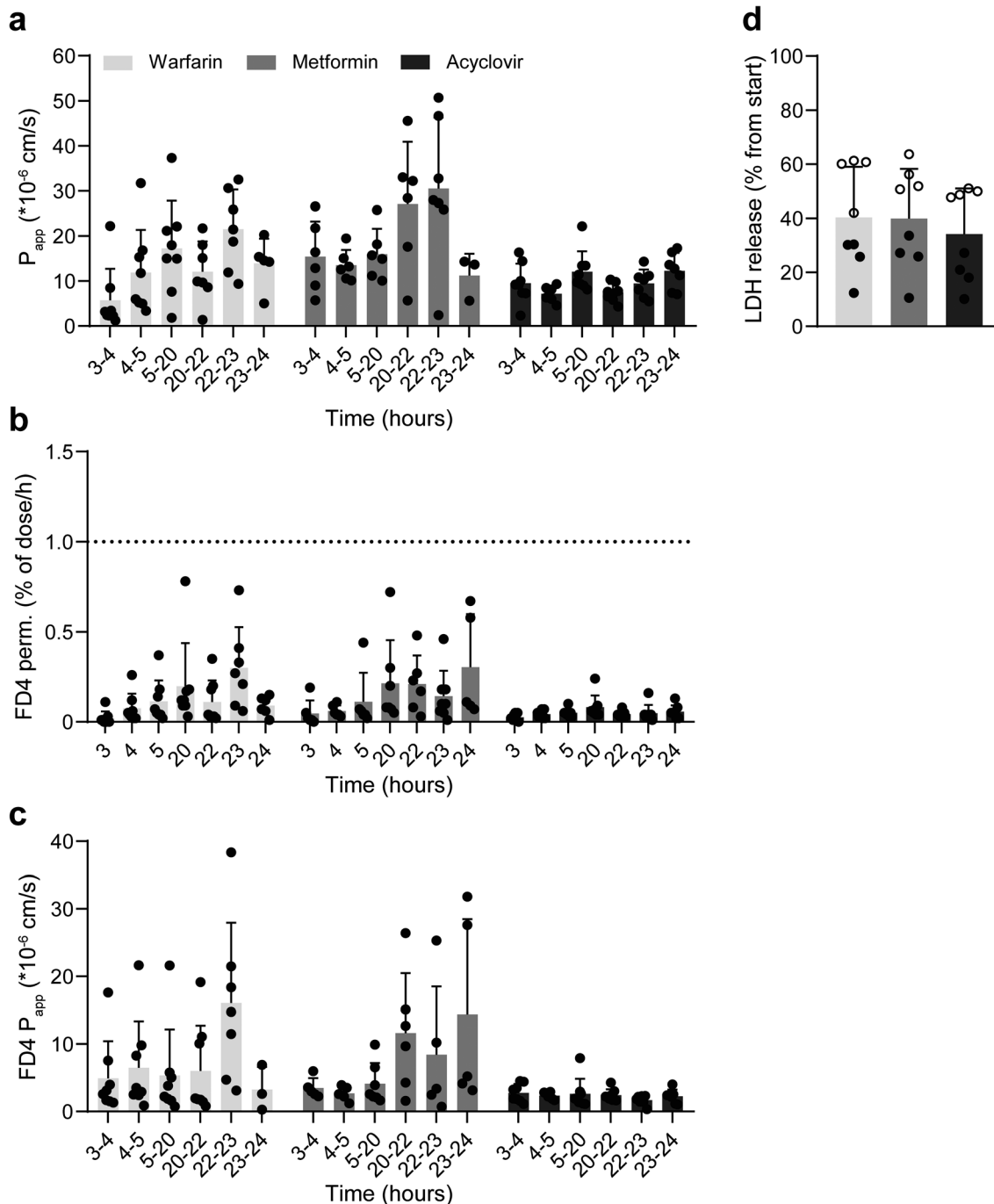
Fig. 6 Permeability of different drugs in the IEBC. a–d, Porcine colon tissue explants were mounted in the IEBC and exposed to a flow rate of 2 mL h^{-1} for 24 hours (n = 7–8/compound, data collected from 2 independent experiments). Warfarin (100 μM), metformin (10 μM) and acyclovir (10 μM) P_{app} (a), FD4 (50 μM) permeability (%/h) (b) and FD4 P_{app} (c) were determined at multiple time points. Dotted line in panel (b) indicates the cut off value of 1%/h. d, Cumulative LDH release into the apical and basolateral compartments was determined after 24 hours and compared to the level of intracellular LDH at t = 0. Data are presented as mean + SD.

donor variation in LDH production and release. Table 2 summarizes the average 3–24 hours P_{app} for warfarin, metformin, acyclovir, atenolol, antipyrine, caffeine and mannitol in human and porcine colon tissue (data Fig. 4b and c, Fig. 5b and c system 2 and Fig. 6a and S5d and e†). Porcine caffeine and mannitol P_{app} were obtained from additional experiments using the setup of system 2 (Fig. 5a).

With a close similarity between porcine and human colon tissue, P_{app} values ranged from ≈16.8–18.1 × 10^{-6} cm s^{-1} for high permeability drugs antipyrine and caffeine to ≈5.4–11.8 × 10^{-6} cm s^{-1} for low permeability drugs atenolol, acyclovir and mannitol. With the exception of metformin, the average 3–24 hours P_{app} values roughly followed the high to low permeability ranking order based on the Fa.[40]

Table 2 Apparent permeability ($P_{app} \times 10^{-6}$ cm s^{-1}) of selected compounds in the IEBC using porcine or human colon tissue

Test compound	% Fa	FDA class	BSC	$P_{app} \times 10^{-6}$ cm s^{-1} porcine colon	$P_{app} \times 10^{-6}$ cm s^{-1} human colon
Antipyrine	100.0	High permeability	I	18.1 ± 1.8	16.8 ± 2.2
Caffeine	100.0	Fa > 85%	I	16.8 ± 1.2	18.1 ± 4.6
Warfarin	98.7		II	13.7 ± 2.2	n.d.
Metformin	53.0	Moderate permeability	III	21.1 ± 2.7	n.d.
Atenolol	50.7	Fa = 84–50%	III	9.9 ± 1.4	5.4 ± 0.7
Acyclovir	25.0	Low permeability	III	9.9 ± 0.9	n.d.
Mannitol	19.2	Fa < 50%	III	11.8 ± 0.9	9.9 ± 5.1

Compounds were selected and ranked based on the fraction absorbed. Compounds were incubated at 10 μM (antipyrine, caffeine, metformin, atenolol, acyclovir and mannitol) or 100 μM (warfarin) and the average P_{app} was calculated between 3–24 hours. Data represents mean ± SEM (multiple donors) or SD (single donor). Porcine: $n = 11$ for antipyrine and atenolol (3 donors), $n = 7$–8 for warfarin, metformin, and acyclovir (2 donors), $n = 14$ for caffeine and mannitol (4 donors); human: $n = 10$ for antipyrine and atenolol (4 donors), $n = 3$ for caffeine and mannitol (1 donor).

Discussion

The IEBC is the first microphysiological system to use *ex vivo* tissue to study intestinal drug absorption. Using fresh tissue explants in drug absorption studies instead of single-cell monolayer cultures has clear advantages.[41] Nevertheless, explants are often integrated in a single microchannel in microfluidic devices,[42,43] where a single flow passes the tissue from all sides, mainly due to technical challenges. One of the challenges to hold tissue explants between two compartments, separating the luminal and basolateral sides of the tissue, is to seal the edges of the tissue in such a way that no undesired side leakage occurs between the two compartments. This is especially important in intestinal absorption studies where these cross-contaminations can influence transport results. From a few studies that have been able to establish flow on both sides of tissue explants in microfluidic chips,[34,44] the study by Richardson *et al.*[34] is the most advanced as they used an inert material (cyclic olefin copolymer) for the chip and glued the tissue between two microchannels. Similarly, Dawson *et al.*[44] used "petroleum jelly" to seal the edges of the tissue. Spreadable adhesives change the surface area of the tissue, penetrate into the tissue and make the chip operation more difficult. Furthermore, these studies assemble the whole chip, including the connections, at the moment of integrating the tissue in the chips. The IEBC integrates the tissue between two microfluidic channels with a snap fit mechanism, without the need to assemble the whole chip at the moment of tissue insertions, which makes the integration robust, fast and reproducible without the use of any adhesives. In addition, the exposure area of the tissue in the IEBC remains the same between experiments and can be controlled by changing the dimensions of the fixing insert (Fig. 1). In cell-based organ on a chip devices, cell suspensions are added to microfluidic chips *via* inlets which requires more training and makes the operation of the chip more difficult and time consuming.[45] In the IEBC, the epithelial tissue explants were added to the chip from the top, separated from the inlets and outlets, which is more compatible with conventional methods in cell culture labs and less susceptible to bubble formation in the microfluidic connections.

In drug transport assays, where drug concentrations are low, non-specific adsorption (NSA) of drugs to the materials used in the assay can result in large errors in the analyses.[46–48] In this study, we showed that we can recover more than 86% of seven conventional drugs from the IEBC platform. The partition coefficient (log*P* octanol : water) of the drugs tested, which is a measure for hydrophilicity (negative values) or hydrophobicity (positive values) of molecules, ranged from −3.1 for mannitol to 2.7 for warfarin. The high recovery of the drugs is an advantage of the IEBC compared to the organ on a chip devices that use silicone based materials, mainly polydimethylsiloxane (PDMS) that can absorb small hydrophobic molecules which makes the material less attractive to use in the drug development process.[23,49–51] Recently, many groups have modified the surface properties of PDMS or corrected for the amount of drugs soaked up.[52–54] However, these approaches are not applicable to intestinal drug absorption studies where low concentrations of drugs have to be detected. Furthermore, since we can 3D print with different resins and choose tubing of various materials to minimize the NSA, the IEBC broadens the possibilities to test a variety of compounds with different molecular properties.

Results with human and porcine colon tissue in the IEBC showed that the *ex vivo* intestinal explants remained viable up to at least 24 hours with maintained barrier integrity and a desired ratio of transcellular/paracellular transport. Between the experiments, the total LDH release fluctuated in average between 20–40%, and end segment LDH levels were similar to or slightly lower than the initial amount of LDH present in the tissue. Together with the intact epithelial barrier demonstrated by tissue histology, our LDH results match previous observations obtained with human intestinal explants exposed to dual microfluidic flow.[44] Furthermore, as described by other studies placing *ex vivo* tissues in similar microfluidic devices,[44,55] the release of LDH was highest in the first few hours after inserting the tissue (Fig. S7f†) due to inevitable damage of the tissue by handling, resecting, and

inserting the tissue into the microfluidic chip. Because of the sustained tissue viability in the IEBC experiments we did not expect that nutrient depletion from the medium or waste product accumulation would go beyond limits. This assumption was validated by measuring glucose (nutrient) and lactate (waste product) concentrations in the apical and basolateral media of two representative control experiments using human and porcine colon tissue after 4 and 20 hours of exposure (Fig. S8a and b†). As both Dawson *et al.* and Richardson *et al.* show that tissue viability was endured up to 72 hours in their tissue explant microfluidic systems, it would be interesting to maintain the tissue viability for more than 24 hours in future IEBC studies.

FITC or FITC–dextran conjugates are frequently used to assess the integrity of epithelial barriers *in vitro*. While many studies use large molecular weight FITC–dextran conjugates of ≥20 kDa,[16,18,21,44,56–60] we chose to use a marker molecule with a much smaller molecular weight of 4 kDa. The smaller the molecule used for such measurements, the better it confirms maintained barrier integrity. Furthermore, the 4 kDa FITC–dextran molecule appeared to be a preferred choice to assess intestinal permeability *in vivo*,[61–64] and it was recently demonstrated in a static *ex vivo* tissue model that ≥20 kDa FITC–dextran is unsuitable for barrier integrity assessments.[28] Here, we showed an FD4 leakage of <1% h^{-1}, and in most studies even <0.5% h^{-1}, for intestinal colon tissue explants in the IEBC. These values are in line with the ≈0.3% h^{-1} FD4 leakage observed for human colon tissue explants in the static InTESTine™.[27] Comparisons to other (microfluidic) intestinal tissue explant models are hampered by variations in preparation and incubation of the tissue[28] or FITC(–dextran) molecules of higher or lower molecular weight were used.[34,44] Nevertheless, the IEBC demonstrated lower levels of leakage compared to recently published microfluidic models[34,44] and comparable levels of FD4 leakage to a static multi-well system.[28] Also in comparison to cell-based intestine on a chip devices that used FD4 to assess barrier integrity similar levels of FD4 permeability were shown in the IEBC.[58,65–68] Taken together, these results validate the IEBC application of intestinal tissue explants as a functional barrier model.

The >2 criterion for transcellular/paracellular transport ratio as a marker of tissue functionality, is derived from our previous research with *ex vivo* intestinal tissue mounted in the static InTESTine™ model.[27,29] In those studies, the incubation time was maximally 3 hours. With the IEBC, we showed that this criterion can also be met beyond that timeframe up to 24 hours. Alike Stevens *et al.*,[27] human colon tissue explants demonstrated an antipyrine/atenolol P_{app} ratio larger than 2, as did porcine colon tissue. Although previously a P_{app} ratio above 3 was shown for porcine intestinal tissue by Westerhout *et al.*,[69] it has to be noted that they used intestinal tissue from another region (small intestinal tissue, jejunum) from young piglets, whereas we used colon tissue from adult pigs. It is, therefore, interesting to investigate the influence of age and/or intestinal region on

the transcellular/paracellular ratio in the IEBC in future studies.

The introduction of a 10-fold higher flow rate did not change the transcellular and paracellular transport rates nor the transcellular/paracellular ratio, but it did largely increase the shear stress on the tissue. Assuming water as the working fluid, a colonic diameter range of 35–76 mm[70] and flow rate of 1.5–2 L day^{-1} in the colon,[71] the shear stress falls within the range of $0.56–7.6 \times 10^{-5}$ dyne per cm^2 although these values can get as high as 0.03 dyne per cm^2 for non-Newtonian fluids in the colon.[72] Our fluid flow simulations showed that the shear stress on the tissue segments in the IEBC was 3.5×10^{-4} dyne per cm^2 at the flow rate of 2 mL h^{-1} which is close to the estimated values. This flow rate was therefore preferred in subsequent experiments.

The four different experimental setups comparison supports that the transcellular/paracellular ratio is stably established in the IEBC, regardless of dose timing and sampling timepoints. Even though lower transport rates of the radiolabeled compounds were measured at early timepoints after dose administration, the antipyrine/atenolol P_{app} ratio was >2 from the beginning onwards. The lower transport rates early after dosing might be related to the fact that each system needed ~2.5 hours to completely recirculate the apical and basolateral media (~5 mL medium in each reservoir with a flow rate of 2 mL h^{-1}). As the transport rates stabilized >3 hours after dose administration, we settled on this as the first sampling timepoint in our further experiments. Furthermore, the stabilized P_{app} values indicate that transport continued at a more or less constant speed during the complete length of the experiment and thus not reaching an equilibrium in compound concentration between the apical and basolateral sides of the tissue explants. Additionally, re-administration of apical and basolateral media after 20 h let us to correct for potential technical irregularities, for example air bubbles, occurring during the overnight incubation.

Besides antipyrine and atenolol, caffeine and mannitol were used to determine the transcellular/paracellular transport ratio. Based on the 3–24 hours average P_{app} values, the antipyrine/atenolol ratio was higher than the caffeine/mannitol ratio, mainly due to higher paracellular mannitol permeability compared to atenolol. This is in line with the ratios observed for human colon tissue in the static InTESTine™.[27] Furthermore, the P_{app} values of antipyrine and caffeine in the IEBC were highly comparable to the static data, as was the atenolol P_{app} in human colon tissue. However, the mannitol P_{app} in human tissue and the atenolol and mannitol P_{app} in porcine tissue were ~2-fold higher in the IEBC compared to previously published static data.[27] These discrepancies may be explained by the small number of donors used (for human mannitol), species differences in the transport of low permeability compounds (for porcine mannitol and atenolol), or it might be inherent to the dynamic setting of the IEBC in comparison to the static InTESTine™. When further elucidated, a scenario with adjusted P_{app} ratio criteria for the IEBC can be considered.

As a proof of suitability to discriminate between low, medium and high permeability drugs, three additional small molecule drugs were tested in the IEBC using porcine colon tissue. The high permeability drug warfarin has a comparable Fa to antipyrine and caffeine (Table 2), but shows a slightly lower average P_{app} value between 3–24 hours in the IEBC. In Fa the complete intestinal tract is taken into account, therefore, comparison to the P_{app} of one intestinal region can be inaccurate, especially when transport proteins are involved of which the expression varies along the intestinal tract.[73–75] As warfarin is a substrate of the Breast Cancer Resistance Protein (BCRP) efflux transporter on the apical membrane of the intestinal tissue, it is likely that warfarin is partly pumped back into the apical medium of the IEBC, thus explaining its lower P_{app} value compared to antipyrine and caffeine.[76] This discrepancy between the P_{app} of warfarin, antipyrine and caffeine was also observed in the static InTESTine™, but with a larger difference, demonstrating an effect of flow on BRCP-mediated efflux of warfarin.[27] The warfarin P_{app} under high flow conditions was more comparable to the P_{app} of antipyrine and caffeine, of which the transport was not affected by differences in flow rate. As better sink conditions and higher dissolution are achieved with higher flow rates,[77] warfarin efflux by BCRP potentially has a greater chance at lower flow rates than at higher flow rates. Nonetheless, warfarin P_{app} still shows a good rank order relationship between its Fa *in vivo*, even at the low flow rate. Low permeability drug acyclovir ranks among the other two low permeability drugs, *i.e.* atenolol and mannitol, with a similar average 3–24 hours P_{app} value. Metformin, on the other hand, highly deviates from its moderate permeability rank (53% Fa) as it shows an even higher P_{app} value in the IEBC than the high permeability drugs antipyrine and caffeine. Since the *in vivo* Fa is assessed with much higher metformin doses (mM range) than the concentration used in our experiments (10 μM), together with the observation that metformin absorption is a saturable process,[78] it is likely that permeability is higher and might approach 100% Fa at low concentrations. Nevertheless, static *ex vivo* tissue models Ussing[79] and InTESTine™[27] show P_{app} values of ~6 × 10^{-6} cm s^{-1} when using similar concentrations of metformin as used in our study. Still, those experiments in Ussing and InTESTine™ were short term (up to ~1.5 hours), static and with human intestinal tissue whereas the IEBC experiments ran longer, facilitated fluid flow and in this case used porcine intestinal tissue to assess metformin P_{app}. As the IEBC showed proper ranking of the other six drugs tested, time and more experiments, including testing of additional drugs with medium permeability, drugs prone to efflux by transporters or drugs belonging to BSC class IV, will show if metformin remains the only deviant.

This work focused on the characterization of the IEBC and its application in intestinal drug permeability studies, but as for many other *in vitro* models it has its limitations. One limitation is that contractility of the tissue is not addressed. In studies that apply intestinal tissue explants, usually the outer layers, including the muscle layer, are removed.[27,28,34,37,38,79] Access to the basolateral side of the mucosa is needed to accurately measure drug and nutrient permeability across the intestinal epithelium. Although some organ-on-a-chip models provide mechanical stress to mimic tissue contractions,[56] the IEBC does not apply strain on the tissue. It would however be of interest in future research to apply physiological stretching or assess the expression of genes or proteins involved in contraction. Another limitation of the current setup is that the IEBC does not provide the steep physiological oxygen gradient with the supply of oxygenated blood to the basolateral side of the intestinal epithelium and exposure to the anoxic lumen at the apical side. This means that *in vivo* oxygen is retrieved from the basolateral side only, whereas in the IEBC oxygen is retrieved from both sides. Nevertheless, if oxygen would be supplied to the apical side, these cells are able to consume oxygen even though they are slightly less efficient than the cells located at the basolateral side.[38] For practical reasons we had to insert the oxygen sensor plug from the cap of the chip, thus measuring the oxygen concentrations in the apical medium. It would nevertheless be very interesting to measure the basolateral oxygen consumption. Furthermore, development of an aerobic–anaerobic interface would facilitate a more physiological environment for the intestinal tissue, and thereby also create the possibility to incorporate living gut microbiome which has an abundance of strict anaerobes. A few examples of gut-on-a-chip models with an aerobic–anaerobic interface have been presented in the past years,[80–83] but none of these systems use tissue explants and all are technically challenging to operate. Nevertheless, it would be interesting to create such an interface for the IEBC to incorporate the gut microbiome in future research.

Conclusions

In conclusion, we successfully incorporated intestinal colon tissue explants of human and porcine origin between two microfluidic channels and demonstrated the IEBC as the first microfluidic platform to study intestinal permeability *ex vivo*. The IEBC is, however, not limited to intestinal tissue and explants from other organs (*e.g.* skin or liver slices) can also be integrated in this newly developed chip with a maximum throughput of 28 chips in one experiment so far. In addition, custom-made membranes or scaffolds, with or without cultured (stem)cells, can be integrated into the IEBC to establish a (cellular) barrier between two phases of fluid flow for biological and chemical applications. Furthermore, the sustained tissue viability of the intestinal tissue explants provides us with the unique opportunity to look into processes that need a longer time to initiate, such as the immune response. A combination of the IEBC and the intestinal microbiome can consequently lead to valuable insights into intestinal host–microbe interactions and the effect of potential microbiome-mediated drug metabolism on drug absorption.[84] Considering that *ex vivo* tissue offers

intact 3D architecture, mucus production and cell type diversity, including resident immune cells, the IEBC is clearly advantageous over cell-based microfluidic intestine chips to mimic the (human) intestinal functionalities.

Experimental

Chemicals and assay buffer

[14C]antipyrine was purchased from American Radiolabeled Chemicals Inc., [3H]atenolol, [14C]acyclovir, and [14C] metformin were purchased from Moravek biochemical Inc., [14C]caffeine, [14C]warfarin and [3H]mannitol were purchased from Perkin Elmer Inc. All other chemicals were purchased from Sigma-Aldrich Chemie B.V. unless stated otherwise. Williams E buffer was used according to Stevens et al.[27] Williams E was supplemented with 25 mM D-glucose, 10 mL L^{-1} Glutamax and 10 mL L^{-1} HEPES, gentamycin 50 μg mL^{-1}, amphotericin 25 μg mL^{-1} and stored at 2–10 °C until use. Williams E supplemented with 1% and 4% BSA was used to precoat the system and in the basolateral compartment during an experiment, respectively. One day before the experiment, all media and dosing solutions were placed in a humidified incubator at 37 °C with 5% CO$_2$, 20% O$_2$ and 75% N$_2$.

Design and fabrication of microfluidic system

The microfluidic chips and reservoirs were designed in SolidWorks (Dassault systèmes), and printed using RapidShape S60 LED DLP printer (RapidShape GmbH). Preparation of the resin and the printing process has previously been published.[36] Briefly, 24.5 wt% Urethan Dimethacrylate (UDMA, Esstech), 73.5 wt% ethoxylated (4) bisphenol A methacrylate (Bis-EMA-4, Sartomer Arkema), 2.0 wt% bis(2,3,6-thrimethylbenzoyl)phenyl phosphine oxide (Omnirad 819, IGM Resins) were mixed. After this, 0.02 wt% Quinoline Yellow SS (Solvent Yellow 33) was added to the mixture and magnetically stirred for at least 24 hours. After loading the 3D CAD files to the printer, 4 chips were printed in one print job with a layer thickness of 100 μm. After printing, the parts were washed in a bath of 96% ethanol to remove excess uncured resin and then post cured using UV irradiation in an LC-3DPrint Box (NextDent by 3DSystems) for 10 minutes in a nitrogen atmosphere.

Apical and basolateral microchannels had different reservoirs. They were connected to the chips through tubing. The chip was also connected to a 8 or 16 channel peristaltic pump (Ismatec, VWR) through tubing and coupling connectors. The other end of the pump tubing was connected to a sampling bar (ESI† Fig. S2) which could be placed in the waste or on the lid of the reservoir for flushing or recirculation modes, respectively. Pharmed peristaltic, Tygon LMT 55, Tygon 3350 and PTFE tubing (VWR) were used in the setup. The microchannels were 1 mm high and 14 mm wide in its widest location (ESI† Fig. S2a). The exposed part of the tissue had a diameter of 5.6 mm (area of 0.246 cm^2) and the round area to place the tissue in the chip was 11.5

mm in diameter. The top opening of the chip was 14 mm in diameter. Total size of the chip was 21 mm by 40 mm. The cap of the microfluidic chip was tapered, similar to a luer connector profile. The side walls of the cap were sealed with parafilm and a rubber ring spacer ensured the cap remained in the right height.

Mechanical analyses and flow simulations

For mechanical analysis of the snap fit mechanism, a single flexible cantilever connected to a base was separately drawn in SolidWorks and imported to COMSOL Multiphysics (COMSOL Group). For tensile simulations, where the fixing insert pushes the cantilever from the bottom side of the cantilever hook (Fig. 1c), the base was fixed and the bottom of the hook was loaded with an upward force of 0.9 N to 10.8 N (calculated for each cantilever) for 50 μm to 600 μm deformation of the rubber. The elasticity of the rubber was 65A or 2.4 MPa. Fixing inserts of different thicknesses deform the rubber different amounts, as shown in ESI† Fig. S1.

To measure the mechanical properties of the material, tensile tests were performed on nine printed samples from the same material as the chip (Table S1†). The cross section of the test area of the specimens was 4 mm by 2 mm and had a length of 12 mm (DIN 53504). The average elastic modulus and yield strength of the material were 3730.35 MPa and 32.31 MPa, respectively. To measure the force needed to fix the tissue, simple beam deflection equation was used:

$$\delta_{max} = \frac{FL^3}{3EI}$$

where δ_{max} is the maximum deflection of the cantilevers while inserting the tissue (0.23 mm), F is the force that deflects one cantilever, E is the elastic modulus of the material and I is the second moment of area of the cantilever cross section. The force needed to push the fixing insert in place was the sum of the forces applied on all the cantilevers and the force to deform the rubber. The force to compress the rubber 100 μm with insert #2 (ESI† Fig. S1) was calculated 14.44 N.

For flow simulations, the chip design was imported to COMSOL Multiphysics. Flow was simulated only in the apical channel for 2 and 20 mL h^{-1}. All shear stress data were exported to text files and imported to MATLAB R2019b to plot in graphs. For analytical shear stress, the next formula for the shear stress on the bottom of a rectangular channel was used (derived from the parabolic velocity profile of the laminar flow in a rectangular microchannel):

$$\tau_w = \frac{6\mu}{WH^2} Q$$

where μ is the viscosity of water at 37 °C (0.6913 mPa.s), Q is the flow rate, and W and H are the width and height of the

channel at the location of the tissue, respectively (14 mm and 2.25 mm). To calculate the pressure state in the chip, both the COMSOL Multiphysics simulations and the theoretical calculations, based on Hagen–Poiseuille flow, were used.

Human and porcine intestinal tissue

Human intestinal colon tissue was obtained from 5 human adult patients with different age and bodyweight undergoing surgery for mainly colon carcinoma. Ethical approval for the use of redundant intestinal tissue from surgeries (collected as waste material) was provided by the hospital board (Diakonessenhuis, Utrecht, Netherlands). Prior to surgery, informed consent was asked from the patients. No clinically relevant or identifiable information from the patients was collected. After dissection of the intestinal tissue, the healthy considered tissue, examined by the surgeon or pathologist, was donated for research purposes. Porcine intestinal colon tissue from 3 healthy adult pigs was obtained from a local slaughterhouse. No ethical approval was needed for the collection of intestinal tissue from these animals as the tissue was redundant to the slaughter procedure. Tissue was collected within 15 minutes of the death of an animal and immediately flushed with ice cold supplemented Williams E buffer to remove fecal content. During transportation and preparation in the lab, the tissue was placed in ice cold supplemented Williams E buffer. At the laboratory, fat tissue and the musculo-serosal layer of the mucosal layer was dissected off and round segments of 11.1 mm in diameter (area of 0.968 cm^2) were punched. Mounting of the segments into the IEBC occurred within 4 hours after intestinal tissue collection. All experiments were performed in compliance with Dutch legislation on the use of redundant human (AVG, WMO) and slaughterhouse porcine tissue, and institutional guidelines on handling human and animal tissue regarding safety and security.

Intestinal colon tissue in the Explant Barrier Chip

The microfluidic system and Explant Barrier Chips were prepared one day prior to an experiment. After connecting the individual compartments with tubing, reservoirs were filled and the system was subsequently flushed with 20% biofilm (Umweltanalytik) and PBS. Next, Williams E supplemented with 1% BSA was added for overnight incubation in a humidified incubator at 37 °C with 5% CO$_2$, 20% O$_2$ and 75% N$_2$. Flow rates of 2 and 20 mL h^{-1} were used for overnight incubation and flushing, respectively. The next day, systems were transferred to a working bench. 1 mm thick EPDM rubber rings (Eriks), intestinal tissue segments (mucosal side upwards) on a woven mesh of 170 μm in thickness and 50% open area (Nitex, Sefar) and a fixing insert were clicked in the snap fit mechanism, thereby separating the apical and basolateral compartments of the microfluidic chip. Subsequently, the Williams E supplemented with 1% BSA was replaced by the apical and basolateral media: Williams E supplemented with FD4 and drug compounds or

Williams E supplemented with 4% BSA, respectively. Thereafter, the system was placed back in the incubator and perfused at 2 mL h^{-1} or 20 mL h^{-1}. Apical and basolateral samples were collected from the medium reservoirs, during which the peristaltic pump was stopped briefly. At t = 20 h, apical and basolateral media were replaced with fresh media. At the end of the experiment, systems were removed from the incubator and all media were replaced with PBS. Next, the tissue segments were removed from the Explant Barrier Chips and collected for subsequent analyses. Tubings, chips and reservoirs were flushed and washed with 20% biofilm and 70% ethanol.

Oxygen measurement in the InTESTine Barrier Chip

OXY-4 ST (G2) oxygen meter, polymer optical fibers and mini-luer sensor plugs with PSt7 sensor patches (Presens Precision Sensing GmbH) were used to measure the oxygen in the chip directly on top of the tissue explant. The measurements were non-invasive with a resolution of 0.05% at around 21% of dissolved oxygen. A female mini luer was designed on the cap to host the mini luer sensor plug. The polymer fibers connected the sensor meter to the mini luer plugs (ESI† Fig. S4). The temperature was manually set at 37 °C and the oxygen was measured every minute.

Intestinal tissue permeability measurements

[^{3}H]atenolol or [^{3}H]mannitol (low permeability) and [^{14}C] antipyrine or [^{14}C]caffeine (high permeability) were used as reference markers for the paracellular and transcellular transport route, respectively. [^{3}H]atenolol/mannitol and [^{14}C] antipyrine/caffeine were mixed with non-radiolabeled atenolol/mannitol and antipyrine/caffeine, respectively, to obtain final nominal concentrations of 10 μM in the apical solution with an associated radioactivity of 10 and 1 kBq mL^{-1}, respectively. Transport was measured by taking apical (100 μL) and basolateral (500 μL) samples at indicated timepoints (e.g. 3, 4, 5, 20, 22, 23, and 24 hours). Radioactive labelled compounds were measured using the Tri-Carb 3100TR Liquid Scintillation counter (LSC, Perkin Elmer, Boston Massachusetts, United States) after adding scintillation liquid (Ultima Gold, Perkin Elmer Inc., Boston, Massachusetts, United States) to the apical and basolateral samples. Apical-to-basolateral transport was calculated based on the following equation:

$$P_{app} = \frac{dQ/dt}{A \times C_{api,0}}.$$

P_{app} (cm s^{-1}) denotes the apparent permeability coefficient, dQ/dt indicates the appearance rate of the compound at the basolateral side over time, A is the surface area of the exposed tissue and $C_{api,0}$ is the initial dose concentration of the compound. Resistance of a "porous membrane", reciprocal of its permeability, is proportional to their

thickness and inversely proportional to the porosity.[85] The average porosity of human intestinal tissue and the supporting mesh were around $50 \times 10^{-5}\%$[86] and 50%, respectively. Assuming that the exposure area and thickness are in the same order of magnitude, the resistance of the mesh against the diffusion of solutes was 5 orders of magnitude lower than the resistance of the tissue explant. Therefore, we ignored the effect of the mesh on the permeability. The transcellular over paracellular P_{app} ratio was calculated as P_{app} antipyrine/P_{app} atenolol or P_{app} caffeine/P_{app} mannitol. Besides intestinal permeability, we determined the recovery of these and other radiolabeled test compounds. All [^{3}H]- and [^{14}C]-labeled compounds were mixed with non-radiolabeled compound to obtain final nominal concentrations of 10 μM in the apical solution (100 μM for warfarin) with an associated radioactivity of 10 and 1 kBq mL^{-1} for [^{3}H]- and [^{14}C]-label, respectively. Recovery was calculated as percentage of dose.

Tissue viability measurements

To assess the viability of the *ex vivo* intestinal segments, the cytosolic enzyme lactate dehydrogenase (LDH) was measured in the apical and basolateral supernatants of the two-compartmental model using an LDH kit (Sigma-Aldrich) as previously used.[27,29] Intracellular LDH levels were measured with the same kit, after homogenizing the tissue segments in ice-cold Williams E buffer using a Potter–Elvehjem type Teflon pestle tissue grinder (Braun) for 5 min at 200 rpm. Excreted LDH levels were expressed as percentage leakage of the total intracellular LDH of a blanc intestinal tissue segment which was collected before incubation. To compare intracellular LDH at the start and end of an experiment, the absorbance was corrected for tissue weight. Samples were analyzed using the BioTek Synergy HT microplate reader (BioTek Instruments Inc., Winooski, VT) with an excitation/emission wavelength of 490 nm and 520 nm.

Tissue integrity measurements

To assess the barrier integrity of the tissue, every incubation was co-incubated with FITC Dextran 4000 (FD4) and leakage of FD4 from the apical to basolateral compartment was determined. FD4 was analyzed using a BioTek Synergy HT microplate reader (BioTek Instruments Inc., Winooski, VT) with an excitation/emission wavelength of 485 nm and 528 nm. The acceptance criterion for this parameter is FD4 leakage <1% per hour under control conditions.

Morphological analyses

Formalin-fixed, paraffin-embedded tissue samples, 5 μm-thick sections, were stained with hematoxylin (MilliporeSigma, 51275) and eosin (MilliporeSigma, E4382) (H&E). Digital images were obtained using a 3DHistech P250 scanner at magnification 200×.

Statistical analysis

Data are provided as the mean ± standard deviation or standard error of the mean. Differences between 2 groups were analyzed using 2-tailed Student's t test; 1-way ANOVA with Tukey's or Dunnett's *post hoc* analysis was used for comparisons of multiple groups. Statistical significance was considered at $p < 0.05$, and calculations and graphs were generated using GraphPad Prism 8.0 (GraphPad Software Inc.).

Author contributions

HEA and JMD carried out experiments, together with EW, LP. HEA designed the microfluidic system and together with TD and BI designed different components including the IEBC. BI 3D printed the chips and reservoirs. HEA performed fluid and solid mechanic simulations and with the help of TD. JMD performed mathematical and statistical analyses on the tissue experiments. JMD, EvdS and IN developed the study concept and design. Drafting and initial review of the manuscript were performed by HEA, JMD, EW, BI, LP, LS, TD, IN, JW, RM, IB, EvdS. All authors were involved in analysis and interpretation of data and have read and approved the manuscript.

Conflicts of interest

There are no conflicts to declare.

Acknowledgements

References

1 J. Costa and A. Ahluwalia, *Front. Bioeng. Biotechnol.*, 2019, **7**, 1–14.

2 S. A. Hewes, R. L. Wilson, M. K. Estes, N. F. Shroyer, S. E. Blutt and K. J. Grande-Allen, *Tissue Eng., Part B*, 2020, **00**, 1–14.

3 S. L. Prabu, in *Computer Applications in Drug Discovery and Development*, ed. A. Puratchikody, S. Lakshmana Prabu and A. Umamaheswari, IGI Global, 2019, pp. 1–46.

4 A. A. M. Kämpfer, M. Busch and R. P. F. Schins, *Chem. Res. Toxicol.*, 2020, **33**, 1163–1178.

5 G. B. Hatton, V. Yadav, A. W. Basit and H. A. Merchant, *J. Pharm. Sci.*, 2015, **104**, 2747–2776.

6 J. Yu, R. L. Carrier, J. C. March and L. G. Griffith, *Drug Discovery Today*, 2014, **19**, 1587–1594.

7 P. A. Billat, E. Roger, S. Faure and F. Lagarce, *Drug Discovery Today*, 2017, **22**, 761–775.

8 H. Sun, E. C. Chow, S. Liu, Y. Du and K. S. Pang, *Expert Opin. Drug Metab. Toxicol.*, 2008, **4**, 395–411.

9 V. Meunier, M. Bourrié, Y. Berger and G. Fabre, *Cell Biol. Toxicol.*, 1995, **11**, 187–194.

10 D. P. Chopra, A. A. Dombkowski, P. M. Stemmer and G. C. Parker, *Stem Cells Dev.*, 2010, **19**, 131–141.

11 J. P. Mochel, A. E. Jergens, D. Kingsbury, H. J. Kim, M. G. Martín and K. Allenspach, *AAPS J.*, 2018, **20**, 1–9.

12 J. M. Donkers, H. E. Amirabadi and E. van de Steeg, *Curr. Opin. Toxicol.*, 2020, 135907.

13 R. H. Dosh, N. Jordan-Mahy, C. Sammon and C. L. Le Maitre, *Tissue Eng., Part B*, 2018, **24**, 98–111.

14 J. Huang, Y. Ren, X. Wu, Z. Li and J. Ren, *J. Tissue Eng.*, 2019, **10**, 1–11.

15 S. H. Lee, N. Choi and J. H. Sung, *Expert Opin. Drug Metab. Toxicol.*, 2019, **15**, 1005–1019.

16 A. Bein, W. Shin, S. Jalili-Firoozinezhad, M. H. Park, A. Sontheimer-Phelps, A. Tovaglieri, A. Chalkiadaki, H. J. Kim and D. E. Ingber, *Cmgh*, 2018, **5**, 659–668.

17 M. Kasendra, A. Tovaglieri, A. Sontheimer-Phelps, S. Jalili-Firoozinezhad, A. Bein, A. Chalkiadaki, W. Scholl, C. Zhang, H. Rickner, C. A. Richmond, H. Li, D. T. Breault and D. E. Ingber, *Sci. Rep.*, 2018, **8**, 1–14.

18 W. Shin and H. J. Kim, *Proc. Natl. Acad. Sci. U. S. A.*, 2018, **115**, E10539–E10547.

19 M. J. C. Santbergen, M. van der Zande, A. Gerssen, H. Bouwmeester and M. W. F. Nielen, *Anal. Bioanal. Chem.*, 2020, **412**, 1111–1122.

20 P. de Haan, M. J. C. Santbergen, M. van der Zande, H. Bouwmeester, M. W. F. Nielen and E. Verpoorte, *Sci. Rep.*, 2021, **11**, 1–13.

21 L. Gijzen, D. Marescotti, E. Raineri, A. Nicolas, H. L. Lanz, D. Guerrera, R. van Vught, J. Joore, P. Vulto, M. C. Peitsch, J. Hoeng, G. Lo Sasso and D. Kurek, *SLAS Technol.*, 2020, **25**, 585–597.

22 P. De Haan, M. A. Ianovska, K. Mathwig, G. A. A. Van Lieshout, V. Triantis, H. Bouwmeester and E. Verpoorte, *Lab Chip*, 2019, **19**, 1599–1609.

23 A. W. Auner, K. M. Tasneem, D. A. Markov, L. J. McCawley and M. S. Hutson, *Lab Chip*, 2019, **19**, 864–874.

24 V. S. Shirure and S. C. George, *Lab Chip*, 2017, **17**, 681–690.

25 Z. Luo, Y. Liu, B. Zhao, M. Tang, H. Dong, L. Zhang, B. Lv and L. Wei, *J. Pharmacol. Toxicol. Methods*, 2013, **68**, 208–216.

26 S. Alqahtani, L. A. Mohamed and A. Kaddoumi, *Expert Opin. Drug Metab. Toxicol.*, 2013, **9**, 1241–1254.

27 L. J. Stevens, M. M. H. van Lipzig, S. L. A. Erpelinck, A. Pronk, J. van Gorp, H. M. Wortelboer and E. van de Steeg, *Eur. J. Pharm. Sci.*, 2019, **137**, 104989.

28 T. von Erlach, S. Saxton, Y. Shi, D. Minahan, D. Reker, F. Javid, Y.-A. L. Lee, C. Schoellhammer, T. Esfandiary, C. Cleveland, L. Booth, J. Lin, H. Levy, S. Blackburn, A. Hayward, R. Langer and G. Traverso, *Nat. Biomed. Eng.*, 2020, 1–16.

29 J. Westerhout, E. Van De Steeg, D. Grossouw, E. E. Zeijdner, C. A. M. Krul, M. Verwei and H. M. Wortelboer, *Eur. J. Pharm. Sci.*, 2014, **63**, 167–177.

30 P. M. Van Midwoud, M. T. Merema, E. Verpoorte and G. M. M. Groothuis, *Lab Chip*, 2010, **10**, 2778–2786.

31 L. A. Schwerdtfeger, N. J. Nealon, E. P. Ryan and S. A. Tobet, *PLoS One*, 2019, **14**, 1–17.

32 M. Baydoun, A. Treizeibré, J. Follet, S. B. Vanneste, C. Creusy, L. Dercourt, B. Delaire, A. Mouray, E. Viscogliosi, G. Certad and V. Senez, *Micromachines*, 2020, **11**, 150.

33 M. O. Costa, R. Nosach and J. C. S. Harding, *J. 3D Print. Med.*, 2017, **3**, 0–4.

34 A. Richardson, L. A. Schwerdtfeger, D. Eaton, I. McLean, C. S. Henry and S. A. Tobet, *Anal. Methods*, 2020, **12**, 297–303.

35 A. Dawson, C. Dyer, J. Macfie, J. Davies, L. Karsai, J. Greenman and M. Jacobsen, *Biomicrofluidics*, 2016, **10**, 1–10.

36 H. H. H. Maalderink, F. B. J. Bruning, M. M. R. de Schipper, J. J. J. van der Werff, W. W. C. Germs, J. J. C. Remmers and E. R. Meinders, *Plast., Rubber Compos.*, 2018, **47**, 35–41.

37 F. D. Saraví, T. A. Saldeña, C. A. Carrera, J. E. Ibañez, L. M. Cincunegui and G. E. Carra, *Dig. Dis. Sci.*, 2003, **48**, 1767–1773.

38 G. E. Carra, J. E. Ibáñez and F. D. Saraví, *Int. J. Colorectal Dis.*, 2011, **26**, 1205–1210.

39 H. C. Bittig, A. Körtzinger, C. Neill, E. van Ooijen, J. N. Plant, J. Hahn, K. S. Johnson, B. Yang and S. R. Emerson, *Front. Mar. Sci.*, 2018, **4**, 1–25.

40 FDA, in *Handbook of Pharmaceutical Manufacturing Formulations*, Rockville, MD, 3rd edn, 2020, pp. 27–35.

41 I. C. McLean, L. A. Schwerdtfeger, S. A. Tobet and C. S. Henry, *Lab Chip*, 2018, **18**, 1399–1410.

42 M. Cabello, M. Mozo, B. De la Cerda, C. Aracil, F. J. Diaz-Corrales, F. Perdigones, L. Valdes-Sanchez, I. Relimpio, S. S. Bhattacharya and J. M. Quero, *Sens. Actuators, B*, 2019, **288**, 337–346.

43 N. Ota, G. N. Kanda, H. Moriguchi, Y. Aishan, Y. Shen, R. G. Yamada, H. R. Ueda and Y. Tanaka, *Anal. Sci.*, 2019, **35**, 1141–1147.

44 A. Dawson, C. Dyer, J. Macfie, J. Davies, L. Karsai, J. Greenman and M. Jacobsen, *Biomicrofluidics*, 2016, **10**(6), 064101.

45 X. Wang, D. T. T. Phan, D. Zhao, S. C. George, C. C. W. Hughes and A. P. Lee, *Lab Chip*, 2016, **16**, 868–876.

46 T. Fukazawa, Y. Yamazaki and Y. Miyamoto, *J. Pharmacol. Toxicol. Methods*, 2010, **61**, 329–333.

47 S. Fowler, W. L. K. Chen, D. B. Duignan, A. Gupta, N. Hariparsad, J. R. Kenny, W. G. Lai, J. Liras, J. A. Phillips and J. Gan, *Lab Chip*, 2020, **20**, 446–467.

48 R. S. DeWitte, *Drug Discovery Today*, 2006, **11**, 855–859.

49 T. A. Moore, P. Brodersen and E. W. K. Young, *Anal. Chem.*, 2017, **89**, 11391–11398.

50 N. Li, M. Schwartz and C. Ionescu-Zanetti, *J. Biomol. Screening*, 2009, **14**, 194–202.

51 E. Berthier, E. W. K. Young and D. Beebe, *Lab Chip*, 2012, **12**, 1224–1237.

52 A. Gokaltun, M. L. Yarmush, A. Asatekin and O. B. Usta, *Technology*, 2017, **05**, 1–12.

53 R. Prantil-Baun, R. Novak, D. Das, M. R. Somayaji, A. Przekwas and D. E. Ingber, *Annu. Rev. Pharmacol. Toxicol.*, 2018, **58**, 37–64.

54 L. Wang, B. Sun, K. S. Ziemer, G. A. Barabino and R. L. Carrier, *J. Biomed. Mater. Res., Part A*, 2010, **93**, 1260–1271.

55 S. M. Hattersley, D. C. Sylvester, C. E. Dyer, N. D. Stafford, S. J. Haswell and J. Greenman, *Ann. Biomed. Eng.*, 2012, **40**, 1277–1288.

56 H. J. Kim, D. Huh, G. Hamilton and D. E. Ingber, *Lab Chip*, 2012, **12**, 2165–2174.

57 A. Grassart, V. Malardé, S. Gobba, A. Sartori-Rupp, J. Kerns, K. Karalis, B. Marteyn, P. Sansonetti and N. Sauvonnet, *Cell Host Microbe*, 2019, **26**, 435–444.

58 B. Jing, Z. A. Wang, C. Zhang, Q. Deng, J. Wei, Y. Luo, X. Zhang, J. Li and Y. Du, *Front. Bioeng. Biotechnol.*, 2020, **8**, 1–14.

59 T. Satoh, S. Sugiura, K. Shin, R. Onuki-Nagasaki, S. Ishida, K. Kikuchi, M. Kakiki and T. Kanamori, *Lab Chip*, 2018, **18**, 115–125.

60 Y. Guo, P. Deng, W. Chen and Z. Li, *Micromachines*, 2020, **11**(6), 551.

61 V. Volynets, A. Reichold, G. Bárdos, A. Rings, A. Bleich and S. C. Bischoff, *Dig. Dis. Sci.*, 2016, **61**, 737–746.

62 M. S. Hollemans, J. van Baal, G. de Vries Reilingh, B. Kemp, A. Lammers and S. de Vries, *Poult. Sci.*, 2020, **99**, 6818–6827.

63 M. Jie, H. Lin, Z. He, H. Liu, H. Li and J. M. Lin, *Sci. China: Chem.*, 2018, **61**, 236–242.

64 J. Yang, I. Elbaz-Younes, C. Primo, D. Murungi and K. D. Hirschi, *Sci. Rep.*, 2018, **8**, 1–12.

65 M. Kasendra, R. Luc, J. Yin, D. V. Manatakis, G. Kulkarni, C. Lucchesi, J. Sliz, A. Apostolou, L. Sunuwar, J. Obrigewitch, K.-J. Jang, G. A. Hamilton, M. Donowitz and K. Karalis, *eLife*, 2020, **9**, 1–23.

66 E. Naumovska, G. Aalderink, C. W. Valencia, K. Kosim, A. Nicolas, S. Brown, P. Vulto, K. S. Erdmann and D. Kurek, *Int. J. Mol. Sci.*, 2020, **21**, 1–15.

67 S. H. Kim, M. Chi, B. Yi, S. H. Kim, S. Oh, Y. Kim, S. Park and J. H. Sung, *Integr. Biol.*, 2014, **6**, 1122–1131.

68 M. Chi, B. Yi, S. Oh, D. J. Park, J. H. Sung and S. Park, *Biomed. Microdevices*, 2015, **17**, 1–10.

69 J. Westerhout, S. Bellmann, R. van Ee, R. Havenaar, W. Leeman, E. van de Steeg and H. M. Wortelboer, *J. Food Chem. Nanotechnol.*, 2017, **3**, 111–119.

70 M. A. Khashab, P. J. Pickhardt, D. H. Kim and D. K. Rex, *Endoscopy*, 2009, **41**, 674–678.

71 J. Cremer, I. Segota, C. Y. Yang, M. Arnoldini, J. T. Sauls, Z. Zhang, E. Gutierreza, A. Groisman and T. Hwa, *Proc. Natl. Acad. Sci. U. S. A.*, 2016, **113**, 11414–11419.

72 T. Takahashi, *J. Nutr. Sci. Vitaminol.*, 2011, **57**, 265–273.

73 S. F. C. Vaessen, M. M. H. van Lipzig, R. H. H. Pieters, C. A. M. Krul, H. M. Wortelboer and E. van de Steeg, *Drug Metab. Dispos.*, 2017, **45**, 353–360.

74 G. Englund, F. Rorsman, A. Rönnblom, U. Karlbom, L. Lazorova, J. Gråsjö, A. Kindmark and P. Artursson, *Eur. J. Pharm. Sci.*, 2006, **29**, 269–277.

75 J. Enokizono, H. Kusuhara and Y. Sugiyama, *Drug Metab. Dispos.*, 2007, **35**, 922–928.

76 M. S. Yang, C. P. Yu, P. D. L. Chao, S. P. Lin and Y. C. Hou, *J. Pharm. Sci.*, 2017, **106**, 1419–1425.

77 Z. Gao, *AAPS PharmSciTech*, 2009, **10**, 1401–1405.

78 A. J. Scheen, *Clin. Pharmacokinet.*, 1996, **30**, 359–371.

79 V. Rozehnal, D. Nakai, U. Hoepner, T. Fischer, E. Kamiyama, M. Takahashi, S. Yasuda and J. Mueller, *Eur. J. Pharm. Sci.*, 2012, **46**, 367–373.

80 S. Jalili-Firoozinezhad, F. S. Gazzaniga, E. L. Calamari, D. M. Camacho, C. W. Fadel, A. Bein, B. Swenor, B. Nestor, M. J. Cronce, A. Tovaglieri, O. Levy, K. E. Gregory, D. T. Breault, J. M. S. Cabral, D. L. Kasper, R. Novak and D. E. Ingber, *Nat. Biomed. Eng.*, 2019, **3**, 520–531.

81 M. Marzorati, B. Vanhoecke, T. De Ryck, M. Sadaghian Sadabad, I. Pinheiro, S. Possemiers, P. Van Den Abbeele, L. Derycke, M. Bracke, J. Pieters, T. Hennebel, H. J. Harmsen, W. Verstraete and T. Van De Wiele, *BMC Microbiol.*, 2014, **14**, 133.

82 P. Shah, J. V. Fritz, E. Glaab, M. S. Desai, K. Greenhalgh, A. Frachet, M. Niegowska, M. Estes, C. Jäger, C. Seguin-Devaux, F. Zenhausern and P. Wilmes, *Nat. Commun.*, 2016, **7**, 11535.

83 J. Zhang, Y.-J. Huang, J. Y. Yoon, J. Kemmitt, C. Wright, K. Schneider, P. Sphabmixay, V. Hernandez-Gordillo, S. J. Holcomb, B. Bhushan, G. Rohatgi, K. Benton, D. Carpenter, J. C. Kester, G. Eng, D. T. Breault, O. Yilmaz, M. Taketani, C. A. Voigt, R. L. Carrier, D. L. Trumper and L. G. Griffith, *Med*, 2020, 1–25.

84 E. Van De Steg, F. H. J. Schuren, R. S. Obach, C. Van Woudenbergh, G. S. Walker, M. Heerikhuisen, I. H. G. Nooijen and W. H. J. Vaes, *Drug Metab. Dispos.*, 2018, **46**, 1596–1607.

85 H. H. Chung, M. Mireles, B. J. Kwarta and T. R. Gaborski, *Lab Chip*, 2018, **18**, 1671–1689.

86 J. Linnankoski, J. Mäkelä, J. Palmgren, T. Mauriala, C. Vedin, A. Ungell, L. Lazorova, P. Artursson, A. Urtti and M. Yliperttula, *J. Pharm. Sci.*, 2010, **99**, 2166–2175.